Rock and Soil Mechanics

Volume 41 | Issue 10 Article 9

3-10-2021

Numerical simulation of failure processes of heterogeneous rock specimens under assumption of invariant spherical stress during stress drop

Qin SHU
College of Mechanics and Engineering, Liaoning Technical University, Fuxin, Liaoning 123000, China

Xue-bin WANG
Institute of Computational Mechanics, Liaoning Technical University, Fuxin, Liaoning 123000, China, wxbbb@263.net

Yang-feng ZHAO
College of Mechanics and Engineering, Liaoning Technical University, Fuxin, Liaoning 123000, China

Xue-yuan BAI
College of Mechanics and Engineering, Liaoning Technical University, Fuxin, Liaoning 123000, China

Rock and Soil Mechanics 2020 41(10): 3465−3472 ISSN 1000−7598
https: //doi.org/10.16285/j.rsm.2020.5077 rocksoilmech.researchcommons.org/journal

Numerical simulation of failure processes of heterogeneous rock specimens under assumption of invariant spherical stress during stress drop

SHU Qin[1], WANG Xue-bin[2], ZHAO Yang-feng[1], BAI Xue-yuan[1]

1. College of Mechanics and Engineering, Liaoning Technical University, Fuxin, Liaoning 123000, China
2. Institute of Computational Mechanics, Liaoning Technical University, Fuxin, Liaoning 123000, China

Abstract: Using the self-developed code based on the SPH (smoothed particle hydrodynamics) method, evolution of the shear bands and acoustic emission events during failure processes of heterogeneous rock specimens under plane strain uniaxial compression is studied. Based on the Mohr-Coulomb criterion with tensile truncation, the stress calculation method of the failed particle is deduced under the assumption that the spherical stress tensor is invariant during the stress drop. Numerical results show that the longitudinal stress-longitudinal strain curves of the specimens with lower homogeneous degrees demonstrate obvious strain hardening and strain softening stages; strain hardening stages of the specimens with higher homogeneous degrees become less obvious with an increase of the homogeneous degree, and post-peak behaviors of specimens are obviously brittle. Stress drops of particles with different cohesions are theoretically analyzed. Results show that stress drops of particles with higher cohesions are not necessarily larger than the particles with lower cohesions. Stress drops are not only related to the cohesions of the particles, but also to the stress states of the particles when they fail. Effects of homogeneous degree on distributions of failed particles are qualitatively analyzed. The analysis shows that as the homogeneous degree increases, failed particles are more likely to form a narrow shear band quickly penetrating the specimen, with almost no particles failed outside the shear band once the specimen is penetrated. Therefore, the number of final failed particles in the specimen is fewer with an increase of the homogeneous degree.

Keywords: rock specimen; smoothed particle hydrodynamics (SPH); uniaxial compression; shear band; acoustic emission; stress drop

1 Introduction

The process of rock deformation and failure is essentially the process of initiation, expansion, interaction and penetration of defects in the rock[1]. In-depth research on the process of rock deformation and failure is not only conducive to the correct understanding of the mechanism of rock deformation and failure, but also has important significance for the prevention of some geological disasters.

Brittle rocks are generally in an unstable state after the stress peak. It is difficult to describe the mechanical response using the classic strain softening model, instead the brittle plastic model is more suitable [2–4].

At present, numerical methods for simulating the deformation and failure process of rocks emerge in continuously. Typical methods include finite element method, finite difference method and discrete element method. In recent years, the meshless method has received great attention and is considered to be superior to the traditional mesh-based finite element method and finite difference method[5]. The mesh-free method avoids the mesh distortion and mesh reconstruction problems of the mesh method, and can effectively simulate large-deformation problems (such as landslides and debris flows).

The SPH (Smooth Particle Hydrodynamics) method belongs to the mesh-free particle method[6–9]. It is a harmonious combination of the Lagrangian formula and the particle approximation method. It was first used for the simulation of astrophysics, and then used for simulation of solid mechanics and fluid mechanics phenomena [10–15].

The Weibull distribution function is often used to characterize the heterogeneity of rocks [16–20]. The SPH method has been used by some scholars to simulate the brittle failure process of heterogeneous rock samples under uniaxial compression. For example, Sun et al.[17] studied the influence of homogeneity on the failure modes, stress−strain curves and acoustic emissions of rock samples; Zhou et al. [1] also studied the influence of homogeneity on the failure modes and stress−strain curves of rock samples; Li et al.[21] studied the deformation characteristics and acoustic emission of rock samples with single defect. All of the above studies adopted the elasto-brittle-plastic constitutive model, but did not clearly clarify which specific stress dropping mode was

Received: 19 January 2020 Revised: 7 August 2020
This work was supported by the National Natural Science Foundation of China (51874162).
First author: SHU Qin，male, born in 1994, PhD candidate, mainly engaged in research on computational solid mechanics. E-mail: 1522144928@qq.com
Corresponding author: WANG Xue-bin, male, born in 1975, PhD, Professor, mainly engaged in research on deformation, failure and stability of engineering materials. E-mail: wxbbb@263.net

used, nor did them reveal the internal relationship between the homogeneity of the rock samples and the failure modes. Under the stress dropping mode with invariant spherical stress, some scholars have used other numerical methods to simulate the brittle failure process of rock samples under uniaxial compression and surrounding rocks in stope. For example, Pan et al. [2] used elastoplastic cellular automata to simulate the type I and type II curves of rock samples under uniaxial compression; Liu et al.[22] simulated the deformation and failure of surrounding rocks in stope using FLAC^{3D}.

Based on the Mohr-Coulomb criterion with tensile strength cut-off, this paper derives the calculation method of particle stresses under failure assuming invariant spherical stress during stress dropping. Under uniaxial compression in plane strain condition, the study of evolution of shear band and acoustic emission in the process of deformation and failure of heterogeneous rock samples was carried out. Theoretical analysis of the degree of stress dropping of particles with different cohesive forces was performed. In addition, the influence of homogeneity on the distribution of damaged particles was qualitatively analysed.

2 Introduction to SPH method

Essentially, the SPH method is a numerical method for solving partial differential equations. In this method, the calculation model is discretized into a finite number of particles having independent masses and occupying independent spaces. The interaction between the particles is realized by a smooth kernel function (kernel function for short). The kernel function not only governs the form of the function approximation and the size of the particle compact support domain but also determines the approximation accuracy of the SPH method [23]. There is an interaction between the particle pairs in the kernel function support domain.

Convert the continuous form of the kernel approximation of the field function and its derivative of the SPH method into a discrete particle summation form:

$$f(\boldsymbol{x}_i)=\sum_{j=1}^{N}\frac{m_j}{\rho_j}f(\boldsymbol{x}_j)W_{ij} \tag{1}$$

$$\nabla\cdot f(\boldsymbol{x}_i)=\frac{1}{\rho_i}\left[\sum_{j=1}^{N}m_j\left[f(\boldsymbol{x}_j)-f(\boldsymbol{x}_i)\right]\cdot\nabla_i W_{ij}\right] \tag{2}$$

where m and ρ are the mass and density of the particle; kernel function $W_{ij}=W(\boldsymbol{x}_i-\boldsymbol{x}_j,h)$; h is the smooth length; and N is the total number of particles in the support domain of particle i.

Use the SPH method to discretize the conservation equations of mass and momentum in the continuum mechanics, then

$$\frac{\mathrm{d}\rho_i}{\mathrm{d}t}=\rho_i\sum_{j=1}^{N}\frac{m_i}{\rho_j}v_{ij}^{\beta}\frac{\partial W_{ij}}{\partial x_i^{\beta}} \tag{3}$$

$$\frac{\mathrm{d}v_i^{\alpha}}{\mathrm{d}t}=\sum_{j=1}^{N}m_j\left(\frac{\sigma_i^{\alpha\beta}+\sigma_j^{\alpha\beta}}{\rho_i\rho_j}-\prod_{ij}\delta^{\alpha\beta}\right)\frac{\partial W_{ij}}{\partial x_i^{\beta}} \tag{4}$$

where superscripts α and β indicate the coordinate directions; when $\alpha=\beta$, $\delta^{\alpha\beta}=1$; when $\alpha\neq\beta$, $\delta^{\alpha\beta}=0$; v is the speed; x is the coordinate; positive value of stress $\sigma^{\alpha\beta}$ represents in tension, otherwise, it represents in compression, refer to literature [5] for the detailed solving process; $\prod_{ij}$ is Monaghan-type artificial viscosity used to solve non-physical numerical oscillations[11].

3 Calculation method of failure particle stress

Brittle rock has the characteristic of rapid decrease in bearing capacity after reaching the yield strength, which is a characteristic that can be better reflected using the elasto-brittle-plastic constitutive model. The brittle stress drop in this constitutive model is a non-incremental mutation, that is, the migration of stress from the initial yield surface to the residual yield surface is completed instantaneously.

Figure 1 schematically shows the stress drop on the plane of normal stress σ and shear stress τ under the assumption of invariant spherical stress. In this paper, the Mohr-Coulomb criterion with tensile cut-off is used as the failure criterion of particles.

The shear failure of the particles is shown in Fig. 1(a). The absolute value of G on the abscissa represents the theoretical tensile strength; φ_0 and φ_1 are the initial internal friction angle and the residual internal friction angle, respectively; and the value of point F on the vertical axis represents the cohesive force c. Assume that the horizontal stress, vertical stress and shear stress of a particle are σ_x, σ_y and τ_{xy}, respectively. When the stress circle determined by points $B(\sigma_y,\ \tau_{yx})$ and $H(\sigma_x,\ \tau_{xy})$ is tangent to the initial yield surface at point A, the particles would undergo shear failure and the stress would undergo brittle drop. The horizontal stress, vertical stress and shear stress after dropping are set to be σ_x', σ_y' and τ_{xy}', respectively, and the stress circle determined by the points $B'(\sigma_y',\ \tau_{yx}')$ and $H'(\sigma_x',\ \tau_{xy}')$ is tangent to the residual yield surface at point A'. The radii of the stress circles before and after the stress drop are set to be r_0 and r_1, respectively, and both circles are centered at point C. It is assumed that there is no rotation of the stress principal axis during the stress dropping. In this way, points B, B' and C would be positioned on the same line. The intersections of the stress circle and the abscissa before the particle stress drops are the first principal stress σ_1 and the third principal stress σ_3, respectively, with $\sigma_1\geqslant\sigma_3$ specified. α is the angle formed between σ_y and σ_1. The stress drop coefficient is set as $k=r_1/r_0$. The r_0, r_1, τ_{xy}', σ_x' and σ_y' are deduced to be

$$r_0 = \sqrt{\left(\frac{\sigma_x - \sigma_y}{2}\right)^2 + \tau_{xy}^2} \tag{5}$$

$$r_1 = \left(\frac{c}{\tan\varphi_0} + \frac{\sigma_x + \sigma_y}{2}\right)\sin\varphi_1 \tag{6}$$

$$\tau'_{xy} = k\tau_{xy} \tag{7}$$

$$\sigma'_x = \frac{\sigma_x + \sigma_y}{2} + k\frac{\sigma_x - \sigma_y}{2} \tag{8}$$

$$\sigma'_y = \frac{\sigma_x + \sigma_y}{2} - k\frac{\sigma_x - \sigma_y}{2} \tag{9}$$

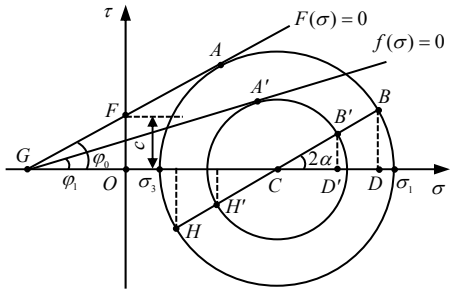

(a) Shear failure

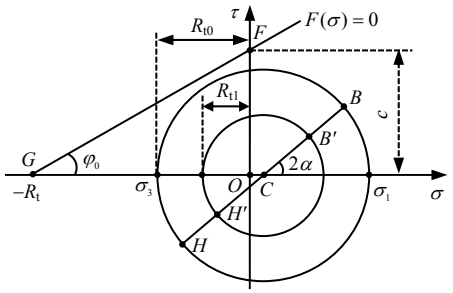

(b) Tensile failure

Fig. 1 Schematic of stress drops under the assumption that the spherical stress is invariant

The tensile failure of particles is shown in Fig.1(b). The tensile failure criterion is considered on the basis of Mohr-Coulomb criterion. Since Mohr-Coulomb criterion usually overestimates the actual tensile strength of the rock, it is necessary to reduce the theoretical tensile strength. According to Mohr-Coulomb criterion, the theoretical tensile strength of particles is $R_t = c/\tan\varphi_0$, and the actual tensile strength after reduction is $R_{t0} = k_1 R_t$, where k_1 is the actual tensile strength coefficient ($0<k_1<1$). When $\sigma_3 + R_{t0} < 0$ is satisfied, the particle would undergo tensile failure; the residual tensile strength would be $R_{t1} = k_2 R_{t0}$, where k_2 is the residual tensile strength coefficient ($0< k_2 <1$). The identical symbols in Fig.1(b) and Fig.1(a) have the same physical meaning, and it is assumed that there is no rotation of the stress principal axis during the stress dropping. The radii of the stress circles before and after the particle stress fall are set to be r'_0 and r'_1, respectively. The stress drop coefficient is set as $k = r'_1/r'_0$. The r'_0 and r'_1 are deduced to be

$$r'_0 = \sqrt{\left(\frac{\sigma_x - \sigma_y}{2}\right)^2 + \tau_{xy}^2} \tag{10}$$

$$r'_1 = \frac{\sigma_x + \sigma_y}{2} - R_{t1} \tag{11}$$

Stress of particles after tensile damage could be obtained by substituting Eqs.(10) and (11) into Eqs. (7)–(9).

4 Calculation model, parameters and scheme

The mechanical model of the rock sample under uniaxial compression is shown in Fig. 2(a). The width of the rock sample is 50 mm and the height is 100 mm. Displacement-control loading was performed at a speed of v=0.2 m/s on the upper boundary of the rock sample while normal constraints were imposed at the lower boundary.

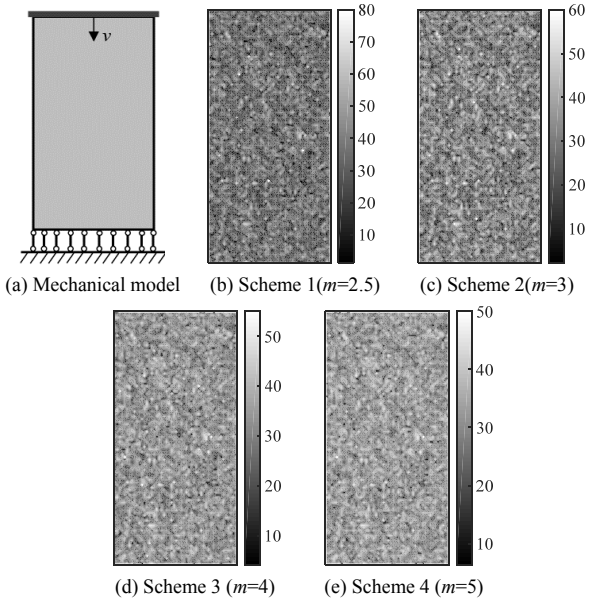

(a) Mechanical model (b) Scheme 1(m=2.5) (c) Scheme 2(m=3)

(d) Scheme 3 (m=4) (e) Scheme 4 (m=5)

Fig. 2 Mechanical model of the uniaxial compressive rock specimen and distributions of c in rock specimens with different schemes (unit: MPa)

The boundary cut-off in the SPH method will affect the calculation accuracy, so the processing of boundary conditions is particularly important. This paper used the mirror virtual particle method[24] to deal with the boundary cut-off problem: the mirror virtual particle and the corresponding real particle have the same density, pressure and stress, and the speed of the mirror virtual particle is obtained by interpolating the corresponding real particle's speed.

The rock sample was discretized into 50×100=5 000 uniformly distributed solid particles, and the distance between adjacent particles in the horizontal and vertical directions is 1 mm. The areal density of the rock is 2 700 kg/m^2, Poisson's ratio μ=0.3, elastic modulus E= 25 GPa, φ_0=30°, φ_1=5°, k_1=1/1.8, and k_2=1/2. The

Weibull distribution function was used to describe the heterogeneity of the rock, and its expression is

$$p(x)=1-\exp\left[-\left(\frac{x}{x_0}\right)^m\right] \quad (12)$$

where $p(x)$ is the probability of variable x; x_0 is the expectation of x; m is the shape parameter, also known as the degree of homogeneity. Assuming that the internal c of the rock sample obeys the Weibull distribution, the expected initial value is 33 MPa. This paper used the same probability distribution to describe the heterogeneity of rocks in different scenarios, that is, the probability of c at the same position of the rock sample in different scenarios is the same.

In this paper, the kernel function proposed in literature [25] was used to eliminate the instability of compressive stress. The smooth length h was taken as 1.2 times the initial spacing of the particles.

The values of m are 2.5, 3, 4 and 5, corresponding to Schemes 1 to 4, respectively. The distribution of c inside the rock sample in each scheme is shown in Figs. 2(b)–2(e). It can be found that the smaller m is, the larger the maximum c inside the rock sample is and the smaller the minimum c is, that is, the more scattered the distribution of c inside the rock sample is; otherwise, these would not be observed.

The calculation was carried out under the conditions of small deformation and plane strain, ignoring the influence of gravity. The Leap-Frog method was used to solve the time integration, where the time step was taken as 1.5×10^{-7} s, and the calculation time is the product of the time step and the number of time steps. A total of 9 000 time steps were calculated.

5 Result analysis

5.1 Rock sample deformation and failure and acoustic emission

Figure 3 shows the longitudinal stress–longitudinal strain curves (referred to as $\sigma_a-\varepsilon_a$ curve) of the rock samples in each scheme. The points a_1–f_1 on the curve correspond to Figs. 4(a)–4(f), respectively. σ_a is the absolute value of the averaged longitudinal stresses of the particles in the top two layers of the rock sample, and ε_a is the product of the calculation time and v divided by the height of the rock sample. It can be found that as m increases, the uniaxial compressive strength σ_c of the rock sample increases, and the corresponding strain ε_c also increases. In addition, when m is small (m=2.5), the rock sample has undergone obvious strain hardening stage and strain softening stage, the rock sample manifests ductile failure; when m is large (m= 3−5), the strain hardening and strain softening process of the rock sample gradually becomes less obvious as m increases, and the rock sample manifests brittle failure.

Due to space limitations, this article only analyses the failure process of the rock sample in Scheme 4 (see Fig. 4). Firstly, it can be found that: just before point a_1, the rock sample has been, for the first time, observed with damaged particles (see Fig.4(a)); during the process from a_1 to b_1, multiple damage particles appeared, and a few damage particles have gathered together (see Fig. 4(b)); then, in the process from b_1 to c_1(σ_c), a large number of damaged particles were connected together to form a shear fracture zone (shear zone) (see Fig.4(c)); during the process from c_1 to d_1, the stress of the rock sample dropped swiftly and the shear zone expanded rapidly (see Fig. 4(d)); finally, as the rock sample continued to deform, the shear zone quickly penetrated the rock sample, and the rock sample experienced brittle failure (see Figs. 4(e)−4(f)). To summarize, the shear zone is formed before the stress peak and rapidly expands until it penetrates the rock sample during the stress drop after the peak.

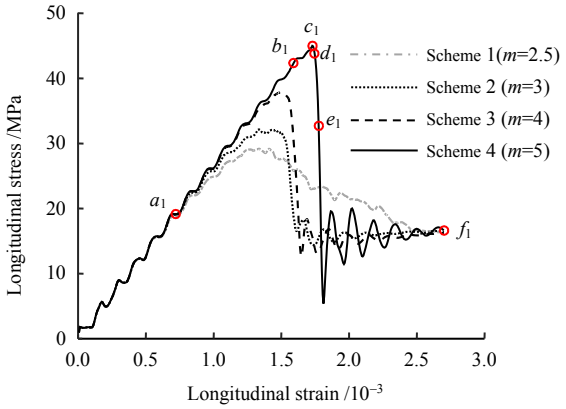

Fig. 3 Longitudinal stress–longitudinal strain curves of rock specimens with different schemes

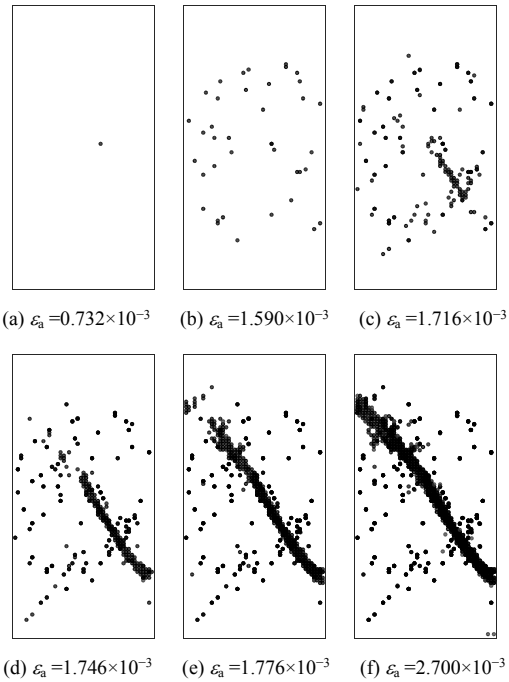

Fig. 4 Failure process of the rock specimen with Scheme 4

For the convenience of description, this paper defines the shear zone that penetrates the rock sample as the primary shear zone, and the rest as secondary shear zones. Figure 5 shows the final (ε_a=2.7×10^{-3}) failure mode of the rock samples in each scheme. It can be seen from Fig. 5:

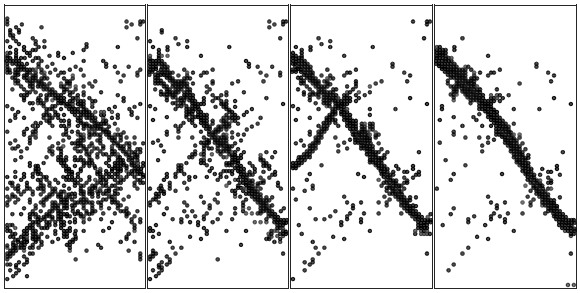

(a) Scheme 1 (b) Scheme 2 (c) Scheme 3 (d) Scheme 4

Fig. 5 Final failure patterns of rock specimens with different schemes

(1) The final failure mode of the rock sample in each scheme contains a straight and right-handed main shear zone, which is related to the same probability setting of *c* at the same position of the rock sample in different schemes. In addition, the final failure modes of the rock samples in Schemes 1 to 3 contain some secondary shear zones.

(2) With the increase of *m*, the distribution of damaged particles changes from a dispersed type to a concentrated type, and the number of damaged particles outside the shear zone shows a decreasing trend. For example, when *m*=2.5, there is a relatively high number of damaged particles outside the shear zone and the distribution is more scattered; when *m*=5, the damage particles are mainly concentrated in the shear zone, and the number of damaged particles outside the shear zone is relatively small.

In this paper, the destruction of each particle is regarded as an acoustic emission (AE) event, and the number of acoustic emission events per 20 time steps (referred to as acoustic emission rate) is counted. Figure 6 shows the evolution of the acoustic emission rate of the rock samples and the cumulative number of acoustic emissions with ε_a, where the circle dot on the ε_a curve with the cumulative number of acoustic emissions is ε_c. In Schemes 1 to 4, before reaching ε_c, with the increase of ε_a, the cumulative number of acoustic emissions gradually increases, and a downward convex trend is showed by the cumulative number of acoustic emissions and the ε_a curve; after reaching ε_c, with the continued increase of ε_a, the cumulative number of acoustic emissions in Scheme 1 gradually increases, the cumulative number of acoustic emissions and the ε_a curve shows a downward concave trend; the cumulative number of acoustic emissions in Scheme 2 firstly increases rapidly then relatively increases, while the cumulative number of acoustic emissions in Schemes 3 and 4 both firstly increases sharply and then slightly increases. As it is well-known that the acoustic emission mode[17, 26] has three main manifestations: swarm shock type, foreshock-mainshock-aftershock type, and mainshock type. Figure 6 shows that: when *m*=2.5, the acoustic emission mode is the swarm shock type; when *m*=3, the acoustic emission mode is the foreshock-mainshock-aftershock type; when *m*=4 and *m*=5, the acoustic emission mode is the mainshock type.

Table 1 provides the statistics of related quantities during the deformation and failure process of the rock samples in each scheme. It can be seen that with the increase of *m*, the maximum values of σ_c, ε_c and the acoustic emission rate all increase, and the maximum values of the acoustic emission rate all appear in the post-peak stage. Prior to ε_c, the cumulative number of acoustic emissions gradually decreases from 318 to 105 with the increase of *m*, and the final cumulative number of acoustic emissions also decreases from 1 082 to 491 with the increase of *m*. In other words, the greater the *m*, the less the final cumulative number of acoustic emissions of the rock sample. The reason will be explained in Section 5.3.

It can also be found from Table 1 that before ε_c, the cumulative number of AE in Scheme 2 accounts for the largest proportion of the final cumulative number of AE, followed by Scheme 1 and Scheme 3, and finally Scheme 4, the reasons for the phenomenon are related to the acoustic emission modes.

5.2 Particle stress drop degree at different *c*

In the numerical simulation of this paper, the rock samples have mainly undergone shear failure with few occurrences of tensile failure. Therefore, the latter will not be considered in the following analysis. In the following, the stress drop degree of particles after shear failure at different *c* is discussed theoretically under the assumption that the Mohr-Coulomb criterion and invariant spherical stress. For the convenience of analysis, take particle 1 and particle 2 as an example for discussion. Among them, the cohesive force of particle 1 (c_1) is smaller than the cohesive force of particle 2 (c_2), and both have the same φ_0 and φ_1. Figure 7 shows a schematic diagram of the stress dropping from the initial yield surface to the residual yield surface of particle 1 and particle 2 on the σ-τ plane. The initial yield surfaces of particle 1 and particle 2 are $F_1(\sigma)=0$ and $F_2(\sigma)=0$, respectively and the residual yield surfaces are $f_1(\sigma)=0$ and $f_2(\sigma)=0$, respectively; the centres of the stress circles are points O_1 and O_2, and the abscissas are $(\sigma_1+\sigma_3)/2$ and $(\sigma_1'+\sigma_3')/2$, respectively.

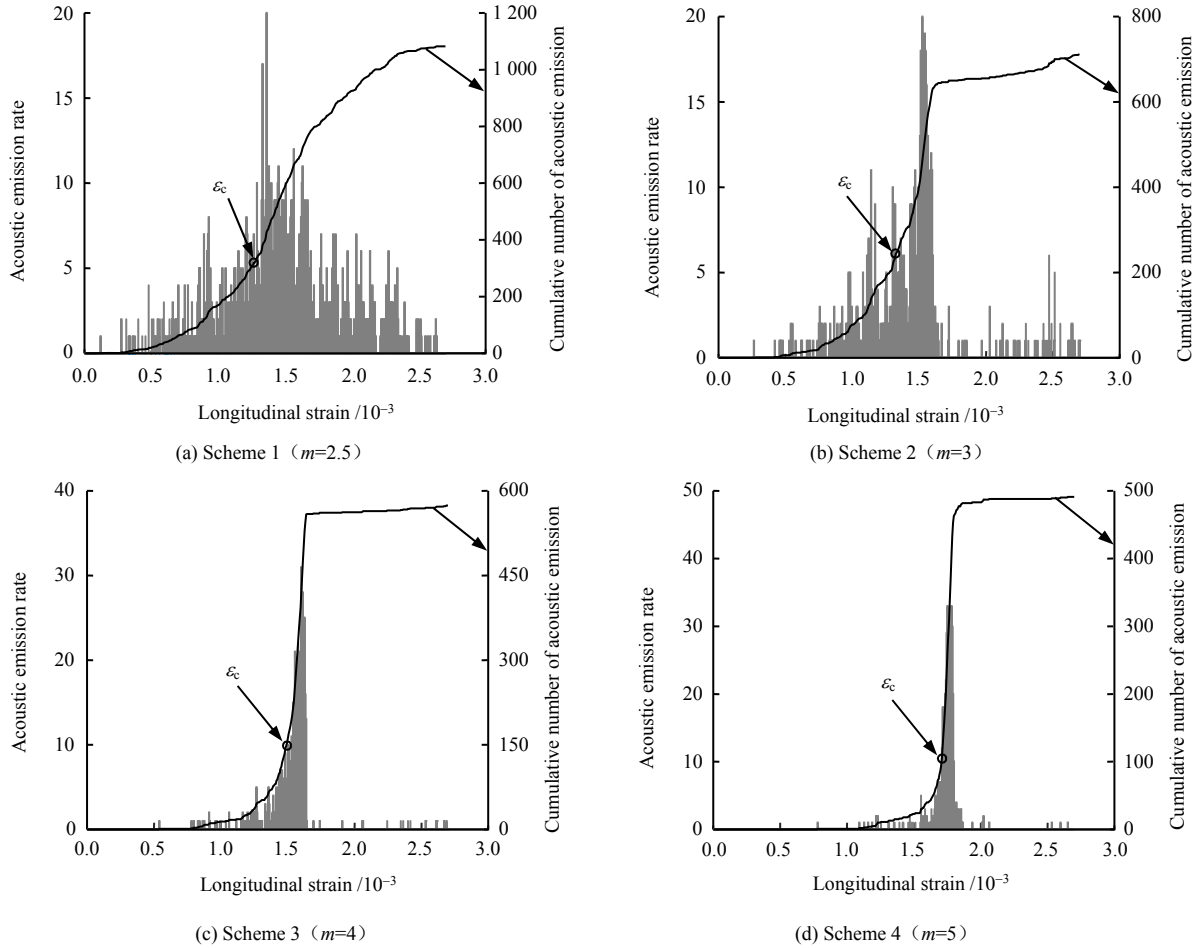

(a) Scheme 1（m=2.5）

(b) Scheme 2（m=3）

(c) Scheme 3（m=4）

(d) Scheme 4（m=5）

Fig. 6 The evolution of the acoustic emission rates and acoustic emission accumulations of rock specimens with ε_a for different schemes

Table 1 Statistics of related quantities during deformation and failure processes of rock specimens for different schemes

Scheme	σ_c/MPa	ε_c/10^{-3}	Maximum value of AE rate	Ratio of ε_a to ε_c corresponding to the maximum AE rate	Cumulative number of AE prior to ε_c	Final cumulative number of acoustic emission	Ratio of cumulative number of AE before ε_c to final cumulative number of AE /%
1(m=2.5)	29.08	1.266	19	1.076	318	1 082	29.39
2(m=3)	32.14	1.332	20	1.153	247	712	34.69
3(m=4)	37.92	1.494	31	1.072	153	574	26.66
4(m=5)	44.99	1.716	33	1.031	123	491	25.05

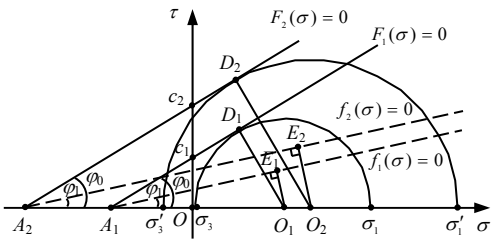

Fig. 7 Stress drops of particles with different c

The radii of the stress circles when the particle reaches the failure condition and after the failure (i.e. after stress drop) are set to as r_0 and r_1, respectively. In order to describe the degree of particle stress drop, the difference between the radii of the stress circles before and after the particle stress drop is defined as $d = r_0 - r_1$, and the greater the d, the greater the degree of the stress drop.

The stress drops of particle 1 and particle 2 are $d_1 = |O_1D_1| - |O_1E_1|$ and $d_2 = |O_2D_2| - |O_2E_2|$, respectively with the difference between the two as $d_{21} = d_2 - d_1$. From the geometric relationship in Fig. 7, there is

$$d_{21} = \left(\frac{\sigma_1' + \sigma_3'}{2} - \frac{\sigma_1 + \sigma_3}{2} + \frac{c_2 - c_1}{\tan\varphi_0} \right) (\sin\varphi_0 - \sin\varphi_1) \tag{13}$$

When $d_{21} > 0$, the stress drop of particle 2 is greater than that of particle 1. Otherwise, it is not. According to the above, $c_2 > c_1$ and $\varphi_0 > \varphi_1$. Therefore, expressions $(c_2 - c_1)/\tan\varphi_0$ and $\sin\varphi_0 - \sin\varphi_1$ on the right-hand-side of Eq.(13) are both greater than 0. There are several possibilities for the sign of d_{21}: (1) When point O_2 is on the right side of the point O_1, or when point

O_2 coincides with point O_1, then $(\sigma_1'+\sigma_3')/2-(\sigma_1+\sigma_3)/2\geqslant 0$, $d_{21}>0$. (2) When point O_2 is on the left side of the point O_1 and satisfies $(\sigma_1'+\sigma_3')/2-(\sigma_1+\sigma_3)/2+(c_2-c_1)/\tan\varphi_0>0$, then $d_{21}>0$. (3) When point O_2 is on the left of point O_1 and satisfies $(\sigma_1'+\sigma_3')/2-(\sigma_1+\sigma_3)/2+(c_2-c_1)/\tan\varphi_0<0$, then $d_{21}<0$. It can be seen that the degree of stress drop after particle failure when c is high is not necessarily greater than that when c is low; the degree of stress drop is not only related to the c of the particle, but also to the stress state (σ_1, σ_3, σ_1' and σ_3') when the particle is damaged. The above results can explain to a certain extent the phenomenon of greater stress drop after particle failure at high c is larger than that at low c.

5.3 Influence of *m* on particle distribution of rock sample failure

Due to stress transfer, the destruction of a particle will cause stress concentration or even destruction of surrounding particles. For analysis simplification, the uniaxial compression is taken as an example, the representative particle i and its neighbouring particles n and k are used for discussion. Figure 8 shows a schematic diagram of the stress redistribution of surrounding particles caused by a certain particle destruction when m is constant, where the abscissa is the particle serial number, the ordinate is σ_1 of the particle (first principal stress), and σ_s is the uniaxial compressive strength of the particle with the expected value being represented by $\bar{\sigma}_s$.

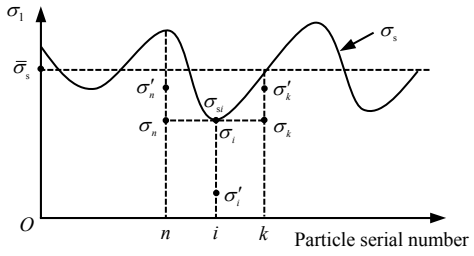

Fig. 8 Schematic of the stress redistribution of surrounding particles caused by a failed particle

As shown in Fig.8, before the particles are destroyed, σ_1 of particles i, n, and k are σ_i, σ_n and σ_k, respectively. Since the three are very close with each other, they can basically be considered the same. Assuming that the uniaxial compressive strength σ_{si} of particle i is the smallest, particle i will be destroyed first. After the particle i is destroyed, the stresses of the particles i, n and k are redistributed and become σ_i', σ_n' and σ_k', respectively. The specific analysis is as follows: when σ_i reaches σ_{si}, the particle i would be destroyed and its σ_1 would drop from σ_i to the residual stress σ_i', and the stress drop $\sigma_i-\sigma_i'$ would be borne by particles n and k. Assuming that particles n and k each bear half of the stress drop, i.e. $(\sigma_i-\sigma_i')/2$, the σ_1 of particles n and k would suddenly rise from σ_i to $(3\sigma_i-\sigma_i')/2$, in other words, σ_n' and σ_k' both equal to $(3\sigma_i-\sigma_i')/2$. When the σ_s of particle n or k is equal or smaller, that is, $\sigma_s\leqslant(3\sigma_i-\sigma_i')/2$, the particle n or k would also be destroyed. Therefore, destruction of the particles n and k mainly depends on their σ_s and $\sigma_i-\sigma_i'$.

When m is large, the fluctuation of σ_s of the particle is small; when m is small, the fluctuation is large. Assuming the same $\bar{\sigma}_s$ of rock samples when m is different, and the residual stress of each particle after failure is σ_i', so that the larger m is, the smaller the absolute value of the difference of σ_s between particle i and particles n and k, and the larger the $\sigma_i-\sigma_i'$. Therefore, the stress is more concentrated in the adjacent particles, the more likely for them to be destroyed. In this way, the distribution of damaged particles is more likely to form a narrow band with a faster expansion of the shear zone. It should also be noted that once the shear zone penetrates the rock sample, the entire rock sample would undergo stress release, and the particles outside the shear band would almost no longer be destroyed after that. Therefore, the final cumulative number of damaged particles of the rock sample would be lower. In addition, the smaller the m is, the larger the number of particles with smaller σ_s is and the more scattered they are distributed, so that the more easily these particles would be destroyed, resulting in the more dispersed distribution of the final damaged particles in the rock sample. The above analysis supports the simulation results in Section 5.1.

6 Conclusions

(1) Based on the Mohr-Coulomb criterion with tensile cut-off, when the stress drops under the assumption of invariant spherical stress, a calculation method of damaged particle stress is deduced. On this basis, the calculation program based on SPH method is developed independently.

(2) The SPH method was used to simulate the deformation and failure process of heterogeneous rock samples under plane strain uniaxial compression. The results show that when the homogeneity is small, the longitudinal stress−longitudinal strain curve of the rock sample presents an obvious strain hardening stage and a strain softening stage; when the homogeneity is large, the strain of the rock sample increases with the increase of homogeneity. The hardening stage becomes less distinct, and the post-peak behavior is obviously brittle.

(3) Under the Mohr-Coulomb failure criterion and the assumption of invariant spherical stress, the theoretical analysis of the degree of stress drop when the cohesive force of particles is different is provided. It shows that the degree of post-failure stress drop when the cohesive force is high is not necessarily greater than that when the cohesive force is low. In addition, the degree of stress drop is not only related to the cohesion of the particles, but also related to the stress state when the particles are

damaged.

(4) Under the assumption that the expected value of the uniaxial compressive strength of the particles and the residual compressive strength are the same, the influence of homogeneity on the distribution of damaged particles is qualitatively analyzed. The result shows that the greater the degree of homogeneity, the greater the degree of stress drop of the damaged particles, the easier it is for the surrounding particles to be damaged, the more accessible it is for the damaged particles to form a narrow shear zone, and the faster the shear zone penetrates the rock sample. The particles outside of the shear zone after the rock sample is penetrated would no longer be damaged. Therefore, the number of final damaged particles of the rock sample is smaller.

References

[1] ZHOU Xiao-ping, ZHAO Yi, QIAN Qi-hu. Numerical simulation of rock failure process in uniaxial compression using smoothed particle hydrodynamics[J]. Chinese Journal of Rock Mechanics and Engineering, 2015, 34(Suppl. l): 2647−2658.

[2] PAN Peng-zhi, ZHOU Hui, FENG Xia-ting. Analysis of mechanism of rock behaviors of classes I and II using elastoplastic cellular automata[J]. Chinese Journal of Rock Mechanics and Engineering, 2006, 25(Suppl. 2): 3823−3829.

[3] SHI Gui-cai, GE Xiu-run, LU Yun-de. Experimental study on coefficients of brittle stress drop of marble[J]. Chinese Journal of Rock Mechanics and Engineering, 2006, 25(8): 1625−1631.

[4] XUE Dong-jie, ZHOU Hong-wei, PENG Rui-dong, et al. Strong disturbance of discontinuous abutment pressure[J]. Chinese Journal of Rock Mechanics and Engineering, 2018, 37(5): 1080−1095.

[5] LIU G R, LIU M B. Smoothed particle hydrodynamics: a meshfree particle method[M]. Singapore: World Scientific, 2003.

[6] LUCY L B. Numerical approach to the testing of the fission hypothesis[J]. Astronomical Journal, 1977, 8(12): 1013−1024.

[7] GINGOLD R A, MONAGHAN J J. Smoothed particle hydrodynamics: theory and application to non-spherical stars[J]. Monthly Notices of the Royal Astronomical Society, 1977, 181(3): 375−389.

[8] CERCOS-PITA J L, ANTUONO M, COLAGROSSI A, et al. SPH energy conservation for fluid-solid interactions[J]. Computer Methods in Applied Mechanics and Engineering, 2017, 317(15): 771−791.

[9] SINNOTT M D, CLEARY P W, MORRISON R D. Combined DEM and SPH simulation of overflow ball mill discharge and trommel flow[J]. Minerals Engineering, 2017, 108: 93−108.

[10] BENZ W, ASPHAUG E. Simulation of brittle solids using smoothed particle hydrodynamics[J]. Computer Physics Communications, 1995, 87(1−2): 253−265.

[11] MONAGHAN J J, KOCHARYAN A. SPH simulation of multi-phase flow[J]. Computer Physics Communications, 1995, 87(1−2): 225−235.

[12] COLAGROSSI A, LANDRINI M. Numerical simulation of interfacial flows by smoothed particle hydrodynamics[J]. Journal of Computational Physics, 2003, 191(2): 448−475.

[13] REN B, WEN H J, DONG P, et al. Numerical simulation of wave interaction with porous structures using an improved smoothed particle hydrodynamic method[J]. Coastal Engineering, 2014, 88(2): 88−100.

[14] ZHAO Yi, ZHOU Xiao-ping, QIAN Qi-hu. Elastoplastic analysis of surrounding rock masses around tunnels using general particle dynamics method[J]. Chinese Journal of Geotechnical Engineering, 2016, 38(6): 1104−1116.

[15] LUO Zhao, WANG Chun. Improved SPH boundary conditions and simulation for large deformation of soil[J]. Chinese Journal of Computational Mechanics, 2018, 35(3): 364−371.

[16] FENG Zeng-chao, ZHAO Yang-sheng. Correlativity of rock inhomogeneity and rock bursy trend[J]. Chinese Journal of Rock Mechanics and Engineering, 2003, 22(11): 1863−1865.

[17] SUN Chao-qun, CHENG Guo-qiang, LI Shu-cai, et al. Numerical simulation of coal uniaxial loading acoustic emission based on SPH[J]. Journal of China Coal Society, 2014, 39(11): 2183−2189.

[18] LIANG Zheng-zhao, GONG Bin, WU Xian-kai, et al. Influence of principal stresses on failure behavior of underground openings[J]. Chinese Journal of Rock Mechanics and Engineering, 2015, 34(Suppl.1): 3176−3187.

[19] CHENG Guo-qiang, ZHAO Fang, SHANG Yong-hui, et al. Simulation of gas seepage in heterogeneous coal seam by SPH method[J]. Journal of China Coal Society, 2016, 41(5): 1152−1157.

[20] FANG Z, HARRISON J P. Development of a local degradation approach to the modeling of brittle fracture in heterogeneous rocks[J]. International Journal of Rock Mechanics and Mining Sciences, 2002, 39(4): 443−457.

[21] LI Shu-cai, SUN Chao-qun, XU Zhen-hao, et al. Numerical simulation of deformation localization for defective rock based on meshless method[J]. Rock and Soil Mechanics, 2016, 37(Suppl. 1): 530−536.

[22] LIU Hong-yong, CHENG Yuan-ping, ZHAO Chang-chun, et al. Constitutive model for elasto-brittle-plastic damage of coal rock mass due to mining and its application[J]. Chinese Journal of Rock Mechanics and Engineering, 2009, 29(2): 358−365.

[23] XU Qing-xin. Study of some impact dynamics problems based on smoothed particle hydrodynamics method[D]. Shanghai: Shanghai Jiao Tong University, 2009.

[24] LIU M B, LIU G R, LAM K Y. Investigations into water mitigations using a meshless particle method[J]. Shock Waves, 2002, 12(3): 181−195.

[25] YANG Xiu-feng, LIU Mou-bin. Improvement on stress instability in smoothed particle hydrodynamics[J]. Acta Physica Sinica, 2012, 61(22): 261−268.

[26] WANG Xue-bin. Numerical simulation of failure processes and acoustic emissions of rock specimens with different strengths[J]. Journal of University of Science and Technology Beijing, 2008, 30(8): 837−843.